Available online at www.sciencedirect.com
ScienceDirect
Comput. Methods Appl. Mech. Engrg. 278 (2014) 499–523
Computer methods in applied mechanics and engineering
www.elsevier.com/locate/cma

Stress-based topology optimization method for steady-state fluid–structure interaction problems

Gil Ho Yoon*

School of Mechanical Engineering, Hanyang University, Seoul, Republic of Korea

Received 15 November 2013; received in revised form 24 May 2014; accepted 30 May 2014
Available online 11 June 2014

Highlights

- We solve the stress based topology optimization considering fluid–structure interaction.
- The singularity issue of the fluid–structure interaction is resolved by the qp-relaxation.
- The maximum von-Mises stress of structures due to fluidic force is constrained.
- The design domain is important because the fluid force is dependent on the design domain.

Abstract

This research developed a new stress-based topology optimization method (STOM) for a steady-state fluid–structure interaction (FSI) problem that minimizes the volume subject to the local stress constraints. Despite numerous studies on STOM, challenging optimization issues related to stress-based topology optimization (TO) procedures for fluid–structure multiphysics systems still exist. Critical issues involved in creating a successful TO for an FSI structure include: the interpolation approach between the fluid equation and the structure equation with respect to locally defined design variables, the mutual multiphysics coupling boundary conditions at dramatically evolving interfacing boundaries, and a clear interpretation of the governing equations and the interaction boundary conditions for spatially varying intermediate design variables. In addition to these three issues, which are related to multiphysics equations, there are three important considerations related to the STOM: the stress singularity issue, the issues of multiple constraints and the highly nonlinear behavior of the stress constraints. To resolve all of the aforementioned issues, we applied a monolithic analysis, integrating the qp-relaxation method and the global p-norm approach. Using the present method, we created optimal layouts that minimize the volume constraining local stress values for a steady-state fluid and structural interaction system.
© 2014 Elsevier B.V. All rights reserved.

Keywords: Stress-based topology optimization; Fluid–structure interaction; Monolithic approach

1. Introduction

Multiphysics simulations of transient or steady-state fluid–structure interactions (FSIs) are an important topic with a very wide range of scientific and engineering applications. The difficulties inherent in important FSIs have led to

* Tel.: +82 222200451.
E-mail addresses: gilho.yoon@gmail.com, ghy@hanyang.ac.kr.

http://dx.doi.org/10.1016/j.cma.2014.05.021
0045-7825/© 2014 Elsevier B.V. All rights reserved.

many numerical analysis procedures that can be categorized as either staggered or monolithic analysis procedures, depending on the differences in the coupling manner between fluid and structure (see [1–4] and the references therein for reviews of various representative numerical analysis procedures for FSI systems). Based on a review of the numerical analysis procedures, we found that many size and shape structural optimization methods for FSI systems do not seriously consider the topological connectivity alternation between the fluidic domain and the structural domain. Indeed, it is difficult to develop a topology optimization (TO) that allows for topological alternations between the fluid domain and structural domain. In [5], a new monolithic approach using the deformation tensor was introduced for the TO of FSI. Subsequent research extended this to include an electro-fluid-thermo-compliant multiphysics actuator design [6]. In [7], Andreasen and Sigmund proposed a saturated poroelastic actuator and FSI problem in poroelasticity for shock absorbers. In [2], dynamically tunable fluidic devices were optimized using the hydrodynamic lattice Boltzmann method by neglecting the structural deformations due to fluidic forces. In [8,9], a TO method for the internal structure of an aircraft wing was presented with and without FSI. In [10], a structural optimization design for composite laminated plates subject to FSI was developed. In [11], the aeroelastic optimization of a membrane micro air vehicle wing was designed through TO. For pressure-loaded problems, many studies have been conducted with using an explicit boundary between the fluid and structure [12–16]. In [17,18], mixed formulation was employed for pressure-loaded problems. In [19], the stress constraint was considered with design-dependent loading. In [20,21], turbulent flow, for which the turbulence model is the RANS Spalart–Allmaras turbulence model, was the primary consideration in connection with the heat transfer problem in TO. This was a novel approach for turbulence TO with OpenFOAM and the FVM-based adjoint sensitivity analysis. In those studies, the authors proposed to add the element density based-damping factor to the nonlinear turbulence model equation to calculate the turbulent viscosity as well as the momentum equations. In [3], David et al. presented an optimization method for designing the optimal layout of flow channels in micro-mixers using the lattice Boltzmann method. In [22,23], topological optimization for micro mixers was developed. In [24], a new TO method for unsteady incompressible Navier–Stokes flows is developed. In addition, many studies regarding fluid-related problems in TO have been conducted [4,8,25–30]. However, to the best of our knowledge, no study has focused on local stress values in an FSI multiphysics system, and many theoretical and numerical issues still need to be resolved [31–43]. Based on the recently developed monolithic analysis approach [5,6] and the STOM theories for linear structures [44–49], we present a new stress-based TO framework for FSI systems.

1.1. Issues related to topology optimization (TO) for fluid–structure interactions (FSIs)

Several important issues need to be addressed for a successful STOM for an FSI system. In a structural TO method, the general procedure begins by optimizing the spatially varying density variables assigned to each finite element as shown in Fig. 1. In the solid isotropic material with penalization (SIMP) method, very weak Young's moduli are assigned to finite elements for void domains, and nominal Young's moduli are assigned to finite elements for structural domains to simulate morphological alternations in pure structural optimization problems for stiff structure or compliant mechanism, as shown in Fig. 2(a). This artificial material usage method is also used for other TO problems with other areas of physics such as thermal, electric, magnetic and fluid physics. Unlike pure structural optimization problems, the TO simulation procedure for FSI systems is complicated and ambiguous because the material properties of the Navier–Stokes equation and the linear elasticity equation, as well as the two governing equations themselves must be interpolated with respect to the assigned density design variables, as shown in Fig. 2(b). Another related complication is that, there is ambiguity in interpolating the governing equations and the coupling boundary conditions for FSI for intermediate design variables; however, this issue is not related to the intermediate design variable, i.e., gray element or postprocessing, after optimization convergence. Because of these mathematically ambiguous conditions, the state-of-the-art staggered or monolithic computational analysis methods developed to date for FSI systems have many difficulties and limitations that restrict the locally defined stress constraints. Although several new analysis and optimization methods have been proposed for STOMs for linear and geometrically nonlinear structures, the STOM issues for this particular multiphysics system remain problematic and require further mathematical and scientific modifications and contributions.

Overcoming the aforementioned interpolation issues for the two governing equations and the intermediate design variables, we based on our previous research, which analyzed the finite element-based monolithic analysis procedure on FSI systems [5,6]. The most important differences between our monolithic analysis and the existing staggered and

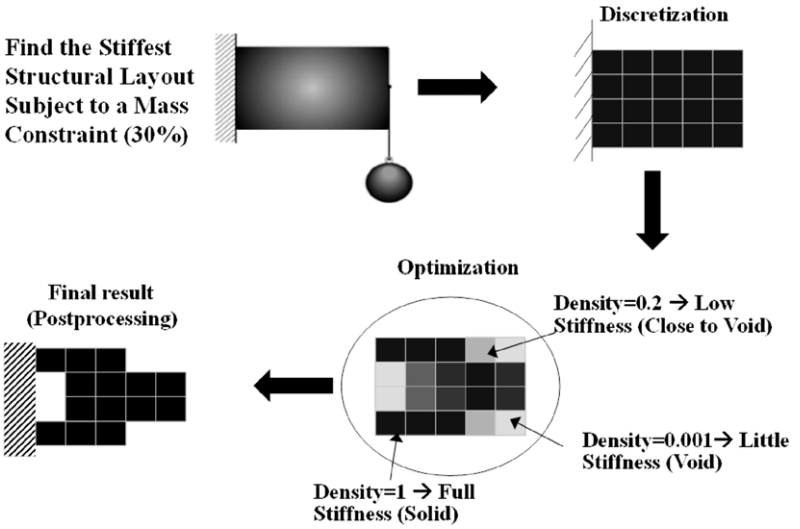

Fig. 1. Topology optimization practice for structural problems.

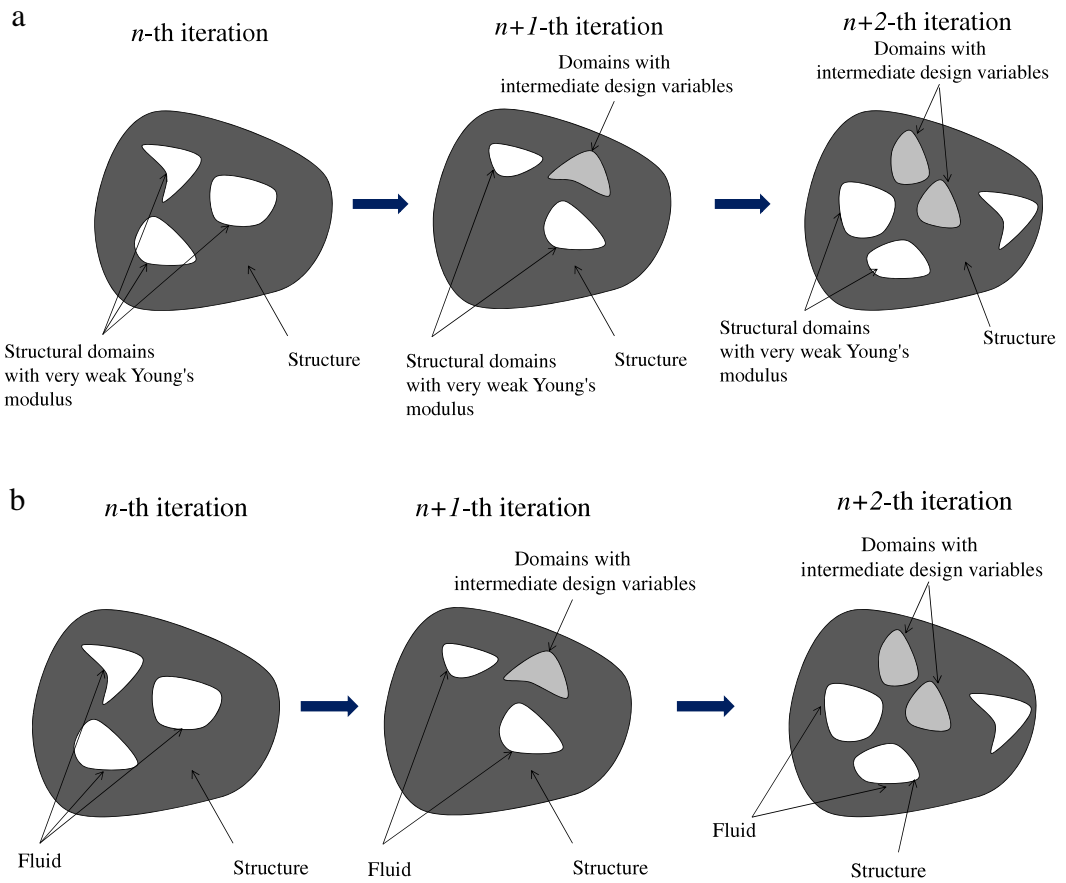

Fig. 2. Difficult issues related to TO of FSIs. (a) Evolution of existing holes for the linear elasticity problem (easy to solve in TO) and (b) evolution of existing holes for FSI problems (issues: interpolating the fluid and the solid equations, imposing the coupling boundary conditions and the unclear domains with intermediate design variables).

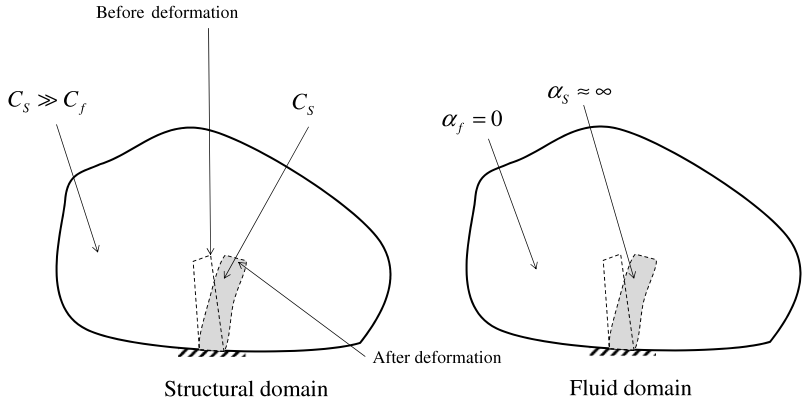

Fig. 3. The monolithic analysis and design method for a steady-state FSI problem without explicit interaction boundaries [5,6]: material values for structural and fluid domains (where C_s and C_f are the Young moduli of the structure and fluid, respectively, and α_s and α_f are the inverse coefficients of the permeability of the solid and fluid, respectively).

monolithic approaches are that the linear elasticity and the Navier–Stokes equation are defined at the unified analysis and design domains and that the interaction boundary conditions are treated as domain forces for the continuity of traction and the clamp condition for the continuity of velocity as shown in Fig. 3. Because the analysis approach proved useful in compliance minimization and multiphysics actuator design problems, e.g., [5,6,50], it is logical to employ this analysis method for the present STOM problem.

1.2. Three inherited issues for STOM: stress singularity, too many constraints and high linear constraints

In addition to the three aforementioned issues, there are additional theoretical issues related to the STOM that need to be addressed to develop a successful STOM for an FSI multiphysics system, namely, the singularity issue, the element wisely defined stress constraint issue and the highly nonlinear constraint issue. The singularity issue in the STOM indicates that the stress constraints defined at the centers of the finite elements of the void domain should be removed at every iteration of the optimization [44,48,51,52]. Many relaxation methods have been proposed to resolve this issue [44–49]; this research implements the *qp*-relaxation method owning to its simplicity and effectiveness. In the *qp*-relaxation method, the penalty parameters of the density design variables for the constitutive matrices for the forward FE analysis and the stress analysis are set differently. Because the fluidic force is only acting on the interacting surfaces and varies depending on the design variables, the basic assumption of the constant force in the STOM is violated. This violation, however, does not adversely affect the applicability of the *qp*-relaxation method to the pure structural optimization problem, i.e., minimizing the volume subject to the stress constraint for a pure elastic structure, for this FSI multiphysics simulation. Furthermore, as the stress constraints are defined at every finite element, an optimization problem with many local stress constraints should be solved by an efficient optimizer [49,53,54]. Many remedies have been proposed, such as the aggregation function [55,56], the p-norm [1], and the segregated global stress norms [36,52,56]. Finally, the highly nonlinear behavior of the stress constraints needs to be addressed [52,57]. To resolve these issues, we implemented previous knowledge, accumulated from the aforementioned related research and various numerical approaches.

This paper is organized as follows. In Section 2, we describe the basic equations for the FSI. In Section 3, we describe our development of the present STOM formulation. In Section 4, we present several numerical examples to show the advantages and disadvantages of the present STOM procedure. In Section 5 we present our conclusions and suggest directions for future research topics.

2. Unified monolithic FE formulation for steady-state FSI

In this section, we review the employed monolithic approach which was basically developed for the TO of the FSI. We first describe all of the formulations, and subsequently explain how we parameterized the involved material parameters for the TO. While minimizing the volume and constraining the local stress values, the fluid and structural

domains inevitably change their shapes continuously, and change their existences discontinuously. This is difficult to model using the existing staggered or monolithic analysis methods in connection with the density-based TO; with the level set-based TO method or the phase field-based TO method which represents topological designs with explicit surfaces, the design changes between solid and fluid may be traceable from an engineering point of view [5,6]. To alleviate these complications, the finite deformation tensor (or the deformation gradient) was introduced to formulate the coupled multiphysics equations that reflect the continuous morphological changes of the fluid and structural domains; the finite deformation tensor, **F**, is one of the basic formulas in continuum mechanics and is defined as the partial differentiation of the current coordinate, **x**, with respect to the undeformed coordinate, **X**. This deformation tensor can be used to correlate the differential operators and the integral operators of the two undeformed/deformed configurations as well as quantities such as mass density, strain, and volume of the two configurations such as shown in (1)–(4).

$$\mathbf{x} = \mathbf{X} + \mathbf{u}, \qquad \mathbf{F} = \frac{\partial \mathbf{x}}{\partial \mathbf{X}} \tag{1}$$

$$\text{Differential operators} : \nabla_{\mathbf{X}} = \mathbf{F}^{\mathrm{T}} \nabla_{\mathbf{x}}, \qquad \nabla_{\mathbf{x}} = \mathbf{F}^{-\mathrm{T}} \nabla_{\mathbf{X}} \tag{2}$$

$$\text{Integral operators} : \int_{{}^{t}\Omega} ()\, d\Omega = \int_{{}^{0}\Omega} () \, \|\mathbf{F}\| \, d\Omega \tag{3}$$

$${}^{0}\Omega = {}_{ms}^{0}\Omega \cup {}_{mf}^{0}\Omega, \qquad {}^{t}\Omega = {}_{ms}^{t}\Omega \cup {}_{mf}^{t}\Omega \, . \tag{4}$$

In the preceding equations, the undeformed fluid domain ${}_{mf}^{0}\Omega$ and the undeformed solid ${}_{ms}^{0}\Omega$ domain are defined inside ${}^{0}\Omega$ and the deformed fluid domain ${}_{mf}^{t}\Omega$ and the deformed solid domain ${}_{ms}^{t}\Omega$ are defined inside ${}^{t}\Omega$. By applying the above finite deformation tensor, the fluid equation for fluid velocities and pressures at the deformed domain ${}^{t}\Omega$ in the monolithic approach can be redefined in the undeformed domain ${}^{0}\Omega$ as follows:

$$-\int_{{}^{0}\Omega} \delta \mathbf{v}^{\mathrm{T}} \left\{ \rho (\mathbf{v} \cdot \mathbf{F}^{-\mathrm{T}} \nabla_{\mathbf{X}} \mathbf{v}) \right\} \|\mathbf{F}\| \, d\Omega = \int_{{}^{0}\Omega} \mathbf{F}^{-\mathrm{T}} \nabla_{\mathbf{X}} \delta \mathbf{v}^{\mathrm{T}} \mathbf{T}_f \, \|\mathbf{F}\| \, d\Omega + \int_{{}^{0}\Omega} \alpha \delta \mathbf{v}^{\mathrm{T}} \mathbf{v} \, \|\mathbf{F}\| \, d\Omega - \int_{{}^{0}\Gamma_{p^*}} p_{p^*} \mathbf{n} d\Gamma \tag{5}$$

$$-\int_{{}^{0}\Omega} \delta p^{\mathrm{T}} \{ (\nabla_{\mathbf{x}} \cdot \mathbf{v}) \} \, \|\mathbf{F}\| \, d\Omega = 0 \tag{6}$$

$$\mathbf{T}_f = -p\mathbf{I} + \mu (\nabla_x \mathbf{v} + \nabla_x \mathbf{v}^{\mathrm{T}}) \tag{7}$$

$$\text{No-slip boundary condition:} \mathbf{v} = \mathbf{0} \quad \text{on } {}_{f}^{t}\Gamma_{\mathbf{v}^0}(\mathbf{u}) \tag{8}$$

$$\text{Inflow/outflow boundary condition:} \mathbf{v} = \mathbf{v}^* \quad \text{on } {}_{f}^{t}\Gamma_{\mathbf{v}^*}(\mathbf{u}) \tag{9}$$

$$\text{Interfacing boundary condition} : \mathbf{v} = \frac{d\mathbf{u}}{dt} (\equiv \mathbf{0} \text{ for steady state flow}) \text{ on } {}_{f}^{t}\Gamma_{i}(\mathbf{u}) \tag{10}$$

$$\text{Pressure boundary condition} : \mathbf{T}_f \cdot \mathbf{n} = p_{p^*} \mathbf{n} \quad \text{on } {}_{f}^{t}\Gamma_{p^*}(\mathbf{u}). \tag{11}$$

Because the derivations and manipulations of the Navier–Stokes equations are lengthy, the final form defined at the undeformed domain ${}^{0}\Omega$ is provided by following the notations in [5,6]. The fluid velocity field and pressure are denoted by **v** and p, respectively and the fluid density and the dynamic viscosity for the Newtonian flow are denoted by ρ and μ, respectively. The Dirichlet boundary conditions are defined along ${}_{f}^{t}\Gamma_{\mathbf{v}^0}$, ${}_{f}^{t}\Gamma_{\mathbf{v}^*}$, and ${}_{f}^{t}\Gamma_{i}(\mathbf{u})$ for the no-slip boundary conditions, inflow/outflow boundary conditions, and interfacing boundary conditions, respectively. With the normal vector **n**, the Neumann boundary condition for the applied pressure, p_{p^*}, is defined at ${}_{f}^{t}\Gamma_{p^*}(\mathbf{u})$. The inverse coefficient of the permeability of fluid is α and is used for the simulation of fluid motions of solid domains, i.e., solid domains of zero velocities, in the TO. With a sufficiently large value of α inside the structural domain and at the coupling boundary, the fluidic velocities approach zero as follows [58]:

$$\begin{cases} \alpha = \alpha_{\max} \gg 0 & \text{for solid or interface boundary} \\ \alpha = 0 & \text{for fluid.} \end{cases} \tag{12}$$

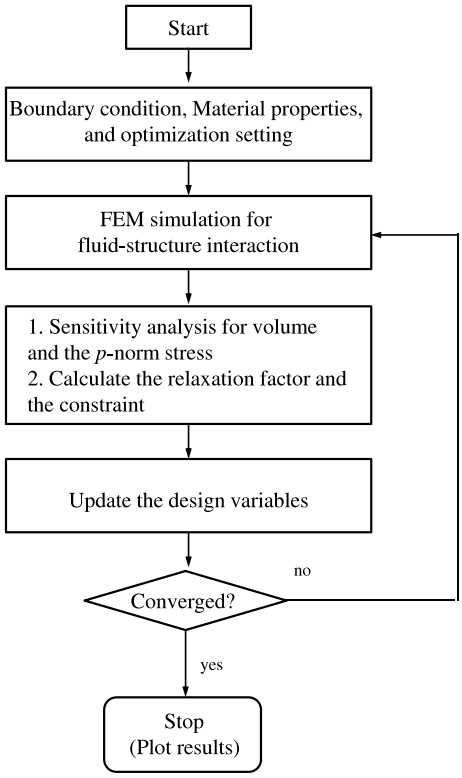

Fig. 4. The developed optimization procedure.

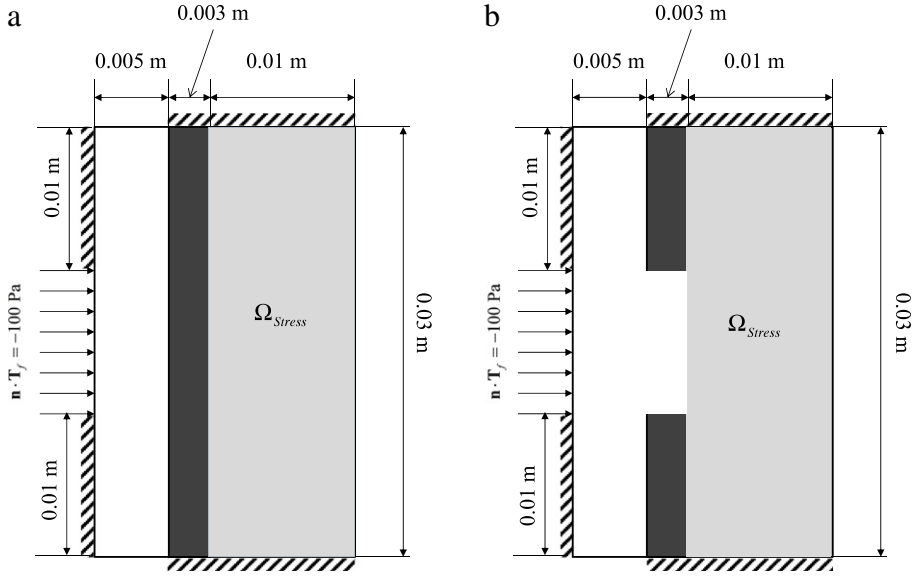

Fig. 5. STOM problem definitions with the pressure input at the center slot at the right side (design domain: gray domain, $\rho = 1000$ kg/m^3, $\mu = 1.002$ Pa s, $C_s = 10\,000$ N/m^2, $\nu = 0.31$, $C_f = C_s \times 10^{-6}$ N/m^2, $\alpha_{\max} = 10^9$).

With the finite deformation tensor in (13), the linear elasticity equation of the deformed domain is transformed into one of the undeformed domain. Because the external elastic energy due to the fluid stress at the coupling boundary is dependent on structural displacements, the deformation tensor is also applied after using the divergence theory for the

Table 1
Interpolated material properties of the present monolithic approach for the FSI problem.

	Linear elasticity equation		Fluid equation
	Young's modulus (C)	Filter for fluid stress (Ψ)	Inverse permeability (α)
Solid	C_s	1	$\alpha \gg 0$
Fluid	$C_f \ll C_s$	0	0

where C_s and C_f are the Young moduli of the solid and fluid, respectively. Young's modulus of the fluid (C_f) is set to a much smaller value than the value of C_s.

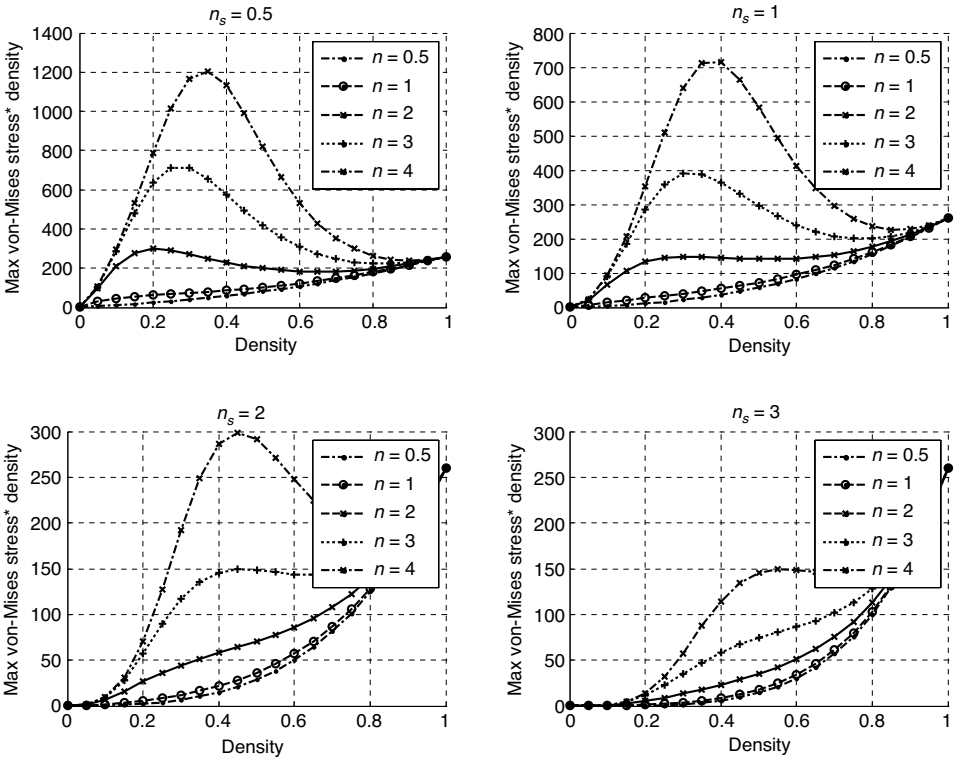

Fig. 6. Maximum von-Mises stress times density with different penalization.

right side of Eq. (13):

$$\int_{0\Omega} \delta \mathbf{S}^{\mathrm{T}} \cdot \mathbf{T}_s d\Omega = \int_{0\Omega} \Psi \cdot \mathbf{F}^{-\mathrm{T}} \delta \mathbf{S}(\mathbf{u}, \delta\mathbf{u})^{\mathrm{T}} \cdot p \, \|\mathbf{F}\| \, d\Omega + \int_{0\Omega} \Psi \cdot \mathbf{F}^{-\mathrm{T}} \delta\mathbf{u} \cdot \nabla_{\mathbf{X}} p \, \|\mathbf{F}\| \, d\Omega \tag{13}$$

$$\Psi = \begin{cases} 1 & \text{for solid domain} \\ 0 & \text{for fluid domain} \end{cases} \tag{14}$$

$$\mathbf{S} = \frac{1}{2}(\nabla_{\mathbf{X}}^{\mathrm{T}}\mathbf{u} + \nabla_{\mathbf{X}}\mathbf{u}), \qquad \mathbf{T}_s = \mathbf{C}\mathbf{S} \tag{15}$$

$$\mathbf{S}(\mathbf{u}, \delta\mathbf{u}) = \frac{1}{2}(\nabla_{\mathbf{x}}^{\mathrm{T}}\mathbf{u} + \nabla_{\mathbf{x}}\mathbf{u}), \qquad \nabla_{\mathbf{x}} = \mathbf{F}^{-\mathrm{T}}\nabla_{\mathbf{X}} \tag{16}$$

where the linear strain $\mathbf{S}$ and the associate stress $\mathbf{T}_s$ are defined above. The linear constitutive matrix is denoted by $\mathbf{C}$. By solving the coupled equations (5) and (6) for the fluid and (13) for the solid, the steady-state FSI system can be analyzed successfully.

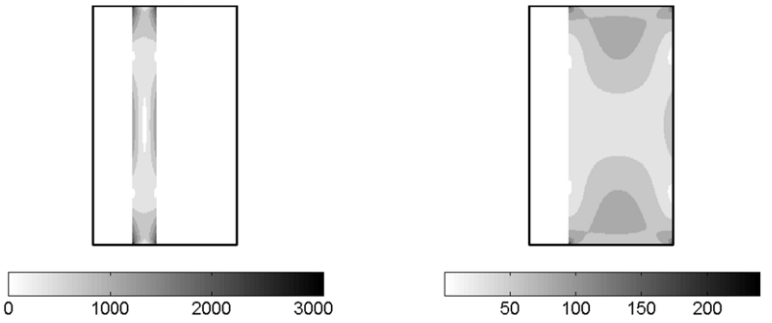

Void Max Von-Mises: 3090.87 Pa Solid Max Von-Mises: 239.59 Pa

(a) Pin = 50 N, Reynolds = 0.7071 for void and 0.3688 for solid.

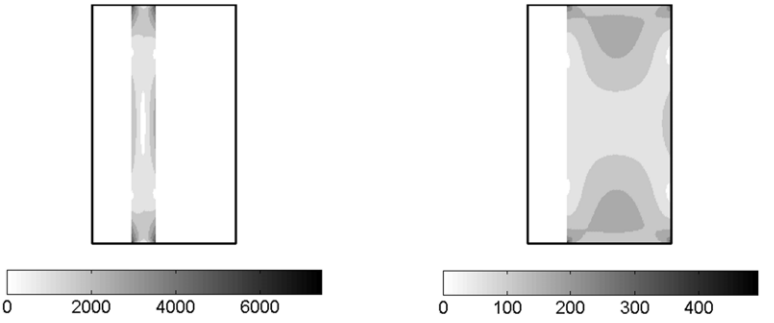

Void Max Von-Mises: 7440.2025 Pa Solid Max Von-Mises: 491.6391 Pa

(b) Pin = 100 N, Reynolds = 1.8808 for void and 0.7756 for solid.

Fig. 7. Maximum and minimum von-Mises stress values and different pressure inputs.

2.1. Interpolation of both physics by interpolating the material properties

The most important feature of the aforementioned monolithic approach is that the mutual coupling analysis of fluid and structure can be accomplished by interpolating Young's modulus of elasticity, the filter Ψ for fluid pressure, and the inverse permeability coefficients listed in Table 1.

3. Stress-based TO formulation

The classical STOM problem can be setup as follows:

$$\begin{aligned} &\underset{\boldsymbol{\gamma}}{\text{Minimize}}\ V(\boldsymbol{\gamma}) = \sum_{e=1}^{NE} \gamma_e v_e \\ &\text{subject to}\ \langle \sigma_{\max} \rangle \leq \sigma^* \end{aligned} \tag{17}$$

$$\langle \sigma_{\max} \rangle^{iter} \equiv c^{iter} \langle \sigma_{PN} \rangle^{iter} \tag{18}$$

$$\langle \sigma_{PN} \rangle^{iter} \equiv \left(\sum_{e} \left(\frac{\sigma_e}{\sigma^*} \right)^p \gamma_e \right)^{1/p} \qquad (e \in [1, 2, \ldots, NE-1, NE]) \tag{19}$$

$$c^{iter} = \alpha_c \frac{\sigma_{\max}^{iter-1}/\sigma^*}{\langle \sigma_{PN} \rangle^{iter-1}} + (1-\alpha_c)\, c^{iter-1}, \quad (0 \leq \alpha \leq 1) \tag{20}$$

$$\sigma_e = \frac{1}{\sqrt{2}} \left[(\sigma_x - \sigma_y)^2 + (\sigma_y - \sigma_z)^2 + (\sigma_x - \sigma_z)^2 + 6\left(\sigma_{xy}^2 + \sigma_{yz}^2 + \sigma_{xz}^2\right) \right]^{1/2}. \tag{21}$$

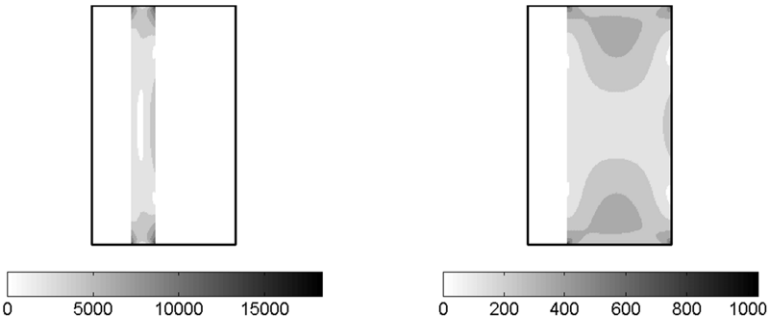

Void Max Von-Mises: 18361.90 Pa Solid Max Von-Mises: 1032.08 Pa

(c) Pin = 200 N, Reynolds = 4.9322 for void and 1.70284 for solid.

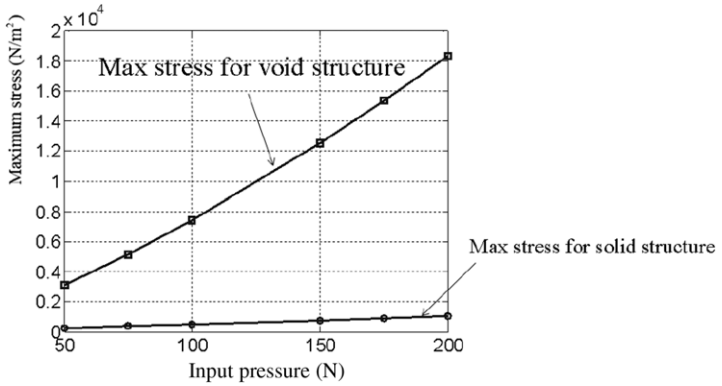

(d)

Fig. 7. (*continued*)

Without a loss of generality, some conventional notations of the finite element method and the TO are used in the aforementioned formulations [31–42,59–64]. The volume of the eth finite element is v_e and the design variables assigned to the NE elements of the design domain are denoted by $\boldsymbol{\gamma}$. The objective function, i.e., volume, is V. To cope with the many constraints issue, the locally defined stress constraints are aggregated by the stress constraints with the stress p-norm $\langle \sigma_{PN} \rangle^{iter}$. Unlike the STOM for linear structures, only one aggregated constraint is used because the STOM for FSI systems with more than one regional constraint makes the TO procedure unstable. In (18), as the p-norm stress is not the real maximum value of the von-Mises stress values, the correction factor c^{iter} is introduced with the damping factor α_c. Our numerical tests show that a real value close to one constrains the inequality stress condition tightly for the first few optimization iterations and then a real value close to zero loosely constrains them for subsequent iterations. In addition, although the maximum stress values are same, depending on the number of elements in Eq. (19), the p-norm values can be different. For example, the p-norm value of [0 0.1 0.2 ... 0.8 0.9 1] becomes 1.2616 with a value of 4 for p, whereas a p-norm value of [0 0.01 0.02 ... 0.98 0.99 1] becomes 2.1279 with a value of 4 for p. This complication concerning the p-norm when attempting to solve the STOM problem can be partially alleviated by a correction factor, namely that the maximum allowable von-Mises stress value σ^*, is provided by engineers to constrain the eth stress value σ_e. Here this value α_c, is set to a real value between 1 and 0.5. Rather than using the p-norm, it may be possible to use the Kreisselmeier–Steinhauser function for the enhanced aggregation method [65].

3.1. qp-relaxation method and the interpolation functions of the SIMP method

In structural TO, the continuous design variable should be adopted to relax the difficult optimization problem, arising from the discrete 0-1 design variable, into an easy optimization problem with a continuous design variable. That is done by varying a small number to one using simple interpolation functions. In the STOM, these interpolation

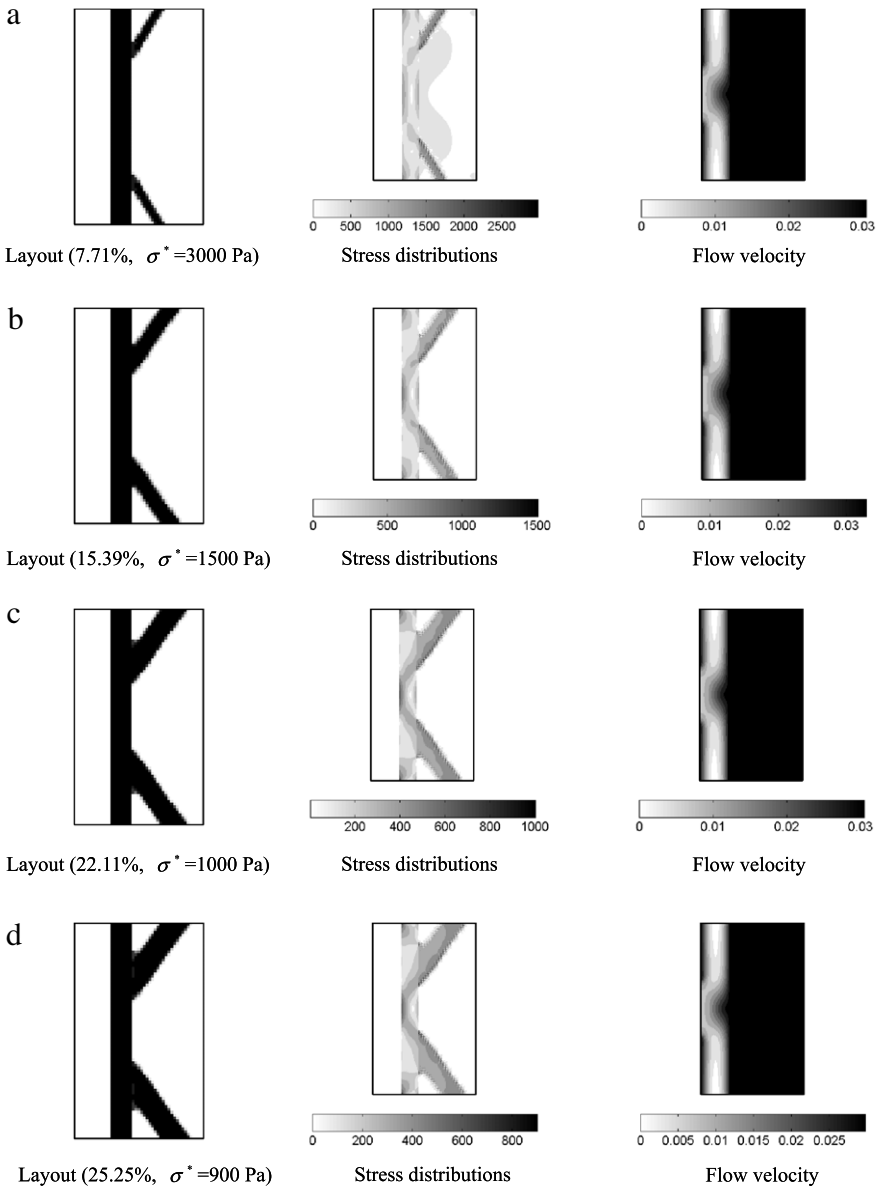

Fig. 8. Optimized layouts constraining the von-Mises stress values in the design domain Ω_{stress} with the separator.

functions should be carefully devised to prevent the stress singularity that makes the TO procedure unstable. To overcome this singularity issue, several innovative approaches have been proposed (see [27,31,42,44–48,52,54]). This research adopted the qp-relaxation approach, which formulates the constitutive matrices for the static and sensitivity analyses for the stress constraints differently, using the simple power laws as follows:

$$\text{Forward analysis} : C_e = \gamma_e^n (C_s - C_f) + C_f \tag{22}$$

$$\text{Sensitivity analysis} : {}_S C_e = \gamma_e^{n_s} (C_s - C_f) + C_f \tag{23}$$

where the penalization factors for the forward analysis and the sensitivity analysis are n and n_s, respectively. The assigned design variable is γ_e for the eth element. To denote the constitutive matrices of the eth finite element for

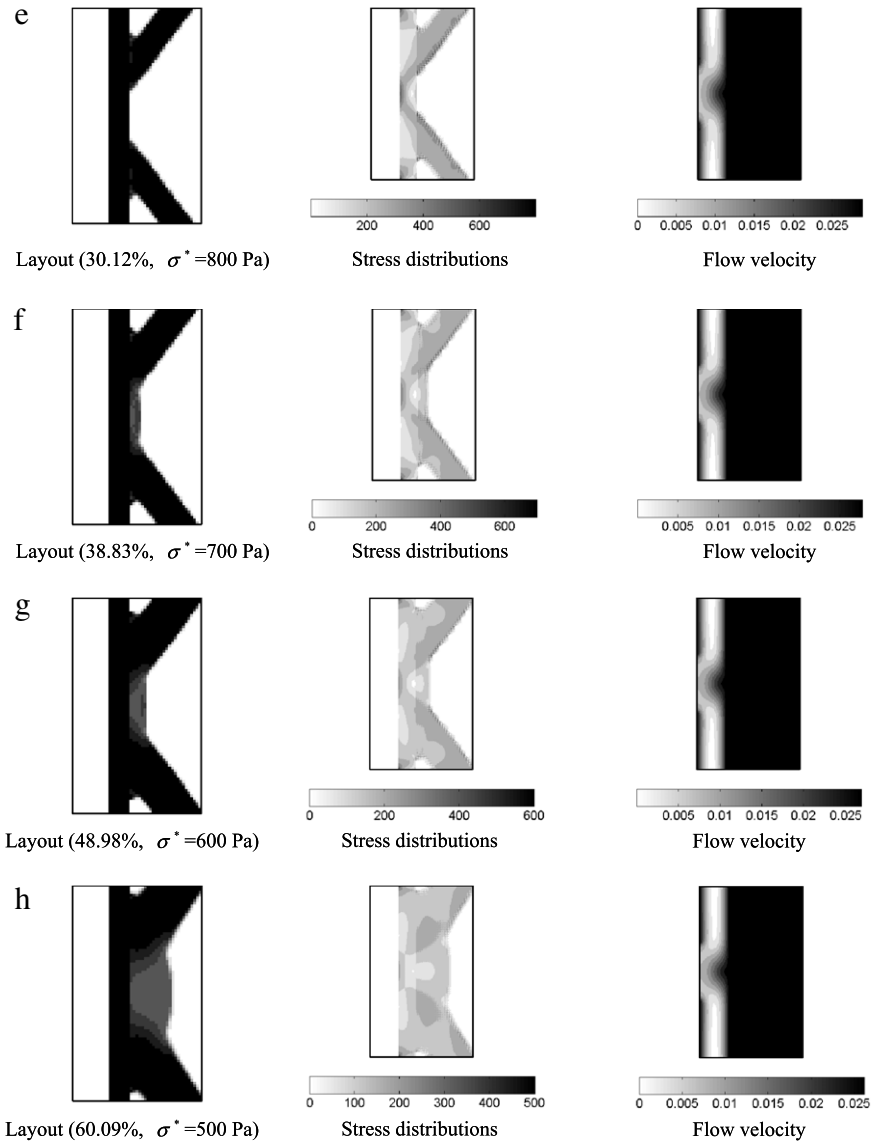

Fig. 8. (*continued*)

the forward analysis and the sensitivity analysis, C_e and ${}_SC_e$ respectively, are used. The constitutive matrices for the solid domain and fluid (void) domain are denoted by C_S and C_f, respectively. In addition, the other functions and properties are interpolated similarly.

$$\Psi = \gamma_e^{n_{filter}} \tag{24}$$

$$\alpha(\gamma_e) = \alpha_{\max}\gamma_e^{n_{per}}. \tag{25}$$

Note that the maximum inverse permeability is denoted by $\alpha_{\max}$ and the penalty factors of the fluid pressure filter and the inverse permeability are denoted by n_{filter} and n_{per}, respectively. Furthermore the polynomial interpolation functions of Eqs. (24) and (25) can be chosen as different functional forms if the physical interpretations of zero and one design variables match with those of the fluid and the solid, respectively.

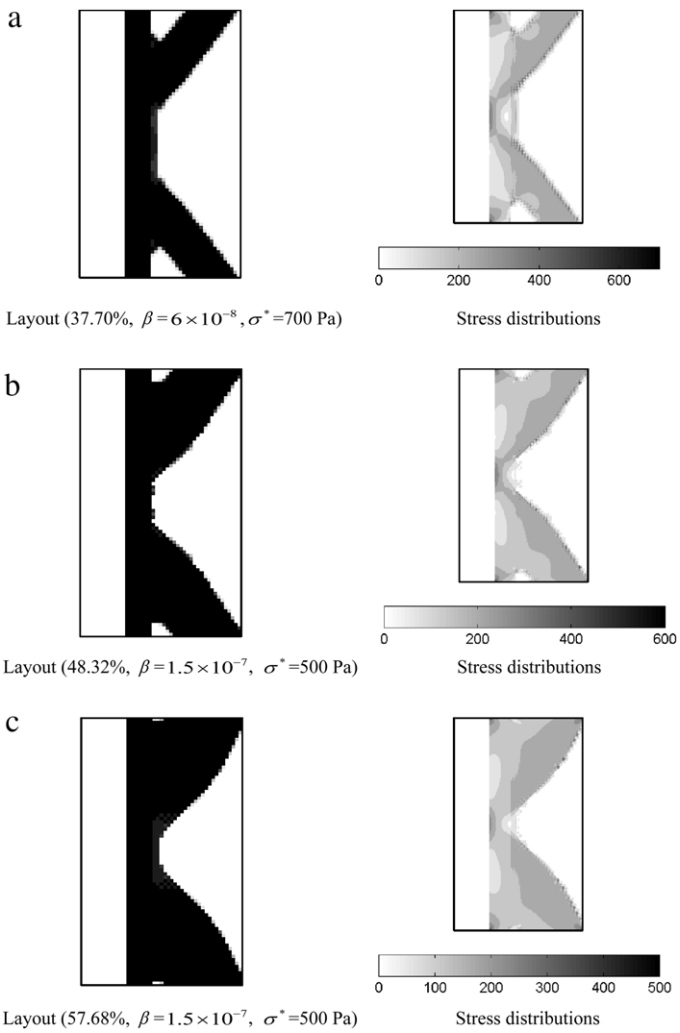

Fig. 9. Optimization results with the penalization for the solid and the void convergence.

4. Optimization examples

This section outlines our solutions to some STOM problems that consider the effects of the FSI to show the validity and limitations of the STOM with the monolithic analysis approach allowing for free material distribution in conjunction with the TO. The adjoint variable method was used for the calculation of the sensitivity values of the global p-norm stress. The element volumes are the sensitivity values of the objective function (volume). For an optimizer, we combined the method of moving asymptotes with the developed analysis codes [66]. The overall procedure is shown in Fig. 4. The material properties and the boundary conditions of the numerical examples are arbitrarily chosen to show the validity of the present approach and the effect of the FSI on optimal layouts.

4.1. Example 1: channel problem

For the first design example, we considered a STOM problem in which a thick elastic bar separated the left fluidic domain (0.001 m × 0.005 m) from the right design domain (0.03 m × 0.01 m) in Fig. 5(a). The design domain is discretized by Q2-P1 fluidic elements satisfying the inf–sup condition and the second order structural plane-strain elements. The objective of TO is to determine an optimal layout that minimizes the volume subject to the local stress constraints at the domain Ω_{stress}, i.e., a STOM for a low Reynolds number flow. Because of the vertical elastic separator and the laminar flow toward the right direction, this optimization problem for Fig. 5(a) becomes relatively

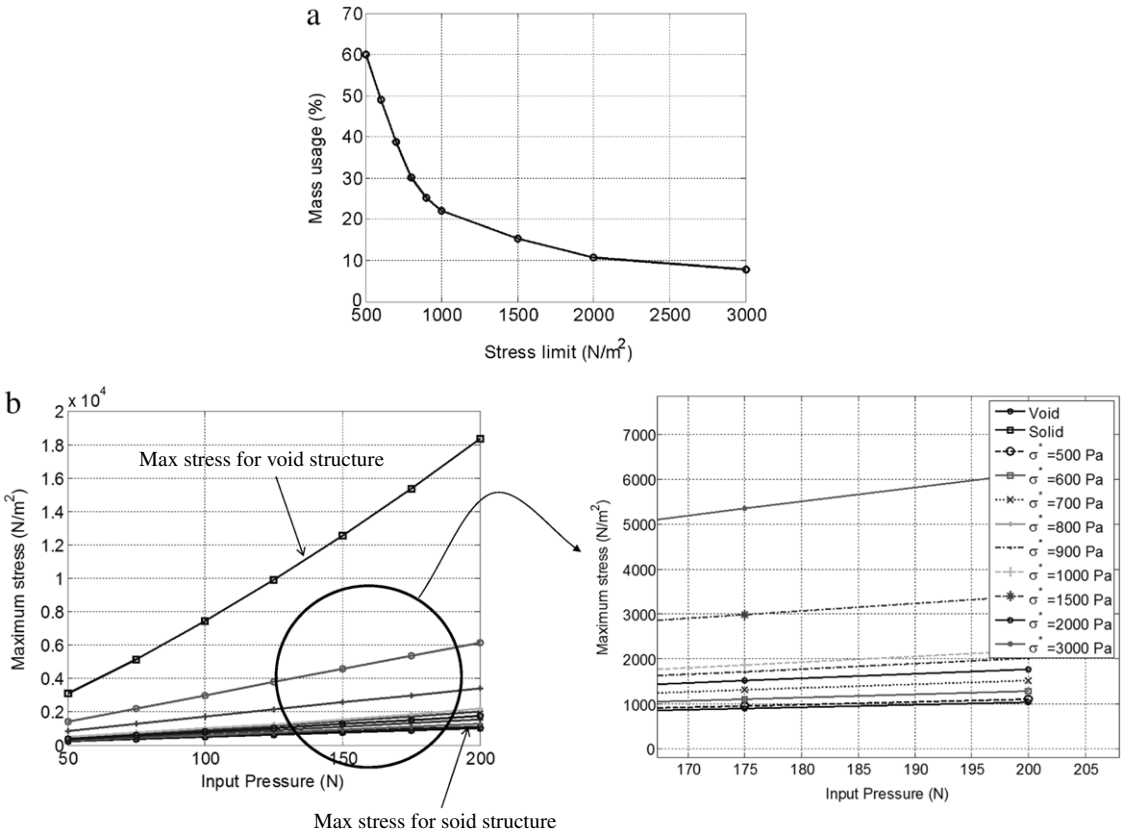

Fig. 10. The relationship between the stress limit and the mass usage and maximum stress values with different pressure inputs.

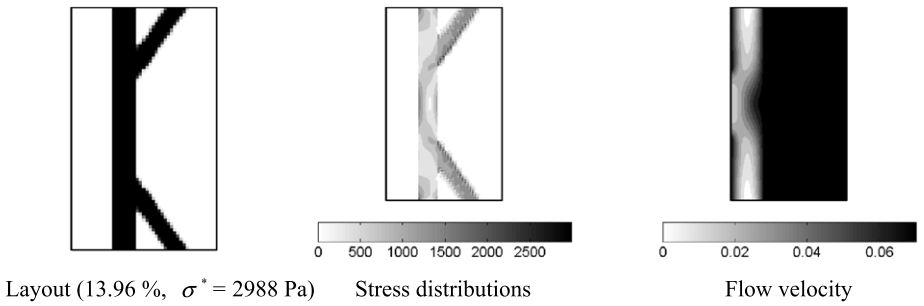

Fig. 11. An optimized layout for a pressure input of 175 Pa, determined by setting the maximum allowable stress to 2988 Pa.

easy to solve. In other words, the fluidic force exerted on the elastic separator do not change significantly with respect to the intermediate designs and an elastic supporting structure should be designed so that it constrains the p-norm mechanical von-Mises stress to a prescribed allowable stress value. To the best of our knowledge, this type of multiphysics STOM design problem has not yet been considered. To test the effects of the penalizations of (22) and (23) in the stress singularity issue, the design variables of the design domain rendered by the gray color are set to a single design variable, and the representative design variable is uniformly varied by void to solid incrementally. The maximum von-Mises stress times the density is plotted in Fig. 6. As observed in the stress-based TO for a pure elastic structure, the penalization factors affect the singularity of this multiphysics system. To resolve the singularity issue, the penalization of Young's modulus in the forward analysis, n, should be set to a higher value than the penalization in the sensitivity analysis, n_s. From our numerical tests, the combinations of the penalization values resulting in their difference to be a high number, i.e., $n - n_s > 2.5$, are recommended.

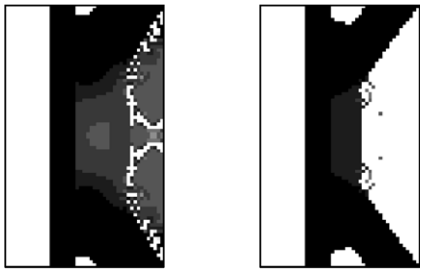

(a) Optimal layout (79.95%, $\sigma^* = 500$ Pa). (b) Optimal layout (49.12%, $\sigma^* = 600$ Pa).

Fig. 12. Sensitivity filtering effect (optimal layouts with the sensitivity filtering).

In the present STOM formulation of (11), it is important to choose an appropriate allowable stress limit. For example, with an unrealistically low stress limit, even a solid structure may not satisfy the stress constraint and with an unrealistically high stress limit, a void structure may be obtained. From out observation concerning the allowable stress limit, the maximum stress values of the solid and the void designs are calculated by varying the input pressure in Fig. 7 for the boundary condition of Fig. 5(a) before solving the STOM for the FSI structure. As expected, the stress values of a solid structure are lower than those of a void structure. Inside the bounded stress region of Fig. 7, some local optimum designs can exist. Based on this, we were able to determine optimum designs for 100 N/m^2 of input pressure in Fig. 8 with various maximum stress limits, ranging from 500 to 3000 Pa, with the simple two bar type design of Fig. 8 supporting the elastic separator, for which the von-Mises stress distributions are similar to that of a sharp triangle structure. By reducing the magnitude of the allowable stress limit, thicker supporting structures with more mass can be obtained. Owing to the limitations of the p-norm approach and the coefficient update-rule in (20), as well as the highly nonlinear constraint, especially with higher penalization factors in (22)–(25), the present designs are local optima and the relationship between the mass usages and the maximum stress limits is plotted in Fig. 10(a). As seen in Fig. 10(b), the maximum von-Mises stress values of the designs for the different pressure inputs are calculated, showing that the stress responses of the designs monotonically increase with respect to the magnitudes of the pressure input. To test the locality of the optimum design, by setting the allowable maximum stress value [i.e., approximately 2988 Pa of the design in Fig. 8(b) for a pressure input 175 Pa], the optimum design in Fig. 11 can be obtained. This design satisfies the constraint and the mass usage is approximately 13.96% and uses less material than Fig. 8(b). However, the layout and the stress responses are similar to the design in Fig. 8(b) and its responses. In Fig. 8(g), there are some intermediate design variables at the right side of the vertical beam. As the design variables interpolate the physics, it is unclear how to interpret these areas. Because the fluid does not penetrate the vertical beam, in this particular case, the area with the intermediate design variables works as the solid domain with the intermediate design variables. To remove this uncertainty, we can add the explicit penalization to the object or the constraint, or it is possible to use the level-set or the phase field-based topology optimization. In this research, to remove the intermediate design variables, one of the easiest way is to introduce the penalization term to the objective function or add the constraint to minimize the number of intermediate design variables.

$$\begin{aligned} &\underset{\boldsymbol{\gamma}}{\text{Minimize}} \;\; V(\boldsymbol{\gamma}) + \sum_{e=1}^{NE} \beta\gamma_e \times (1-\gamma_e) = \sum_{e=1}^{NE} \gamma_e v_e + \sum_{e=1}^{NE} \beta\gamma_e \times (1-\gamma_e) \\ &\text{subject to} \;\; \langle \sigma_{\max} \rangle \leq \sigma^* \end{aligned} \tag{26}$$

where the penalization factor is β. This penalization factor is chosen by trial and error considering the mass volume. With a too large value, some optimal layouts violating the constraint are obtained. The above formulation is applied to some designs of Fig. 8 with intermediate design variables in Fig. 9. As illustrated, the intermediate design variable issue can be partially overcome.

To obtain the aforementioned designs in Fig. 8, we applied the mesh-independent filter to the gradient of the p-norm stress constraint. To test the function of the sensitivity filter in this multiphysics system, we also tested some designs without the sensitivity filters in Fig. 12. In this experiment, some local dots, checkerboards and unusual, small structures appeared, owing to the nonlinearity of the stress constraints and the p-norm stress measure. It is interesting

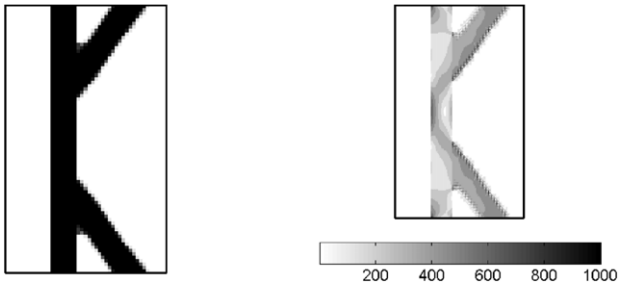

(a) Stress based design layout (mass: 22.11%, $\sigma^* = 1000$ Pa).

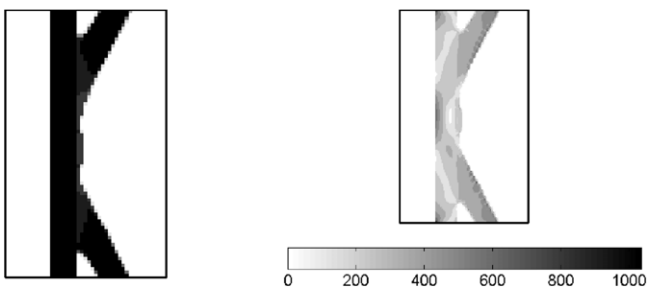

(b) Compliance minimization layout (mass: 22.11%, max stress: 1034 Pa).

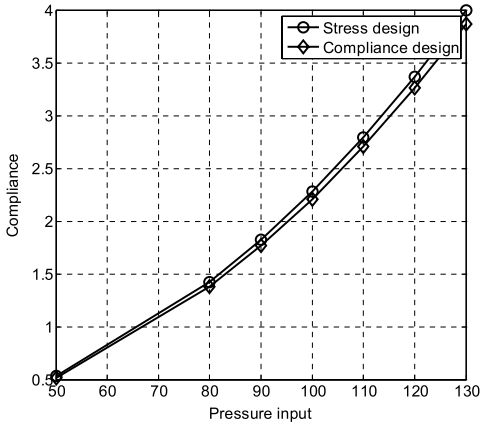

(c)

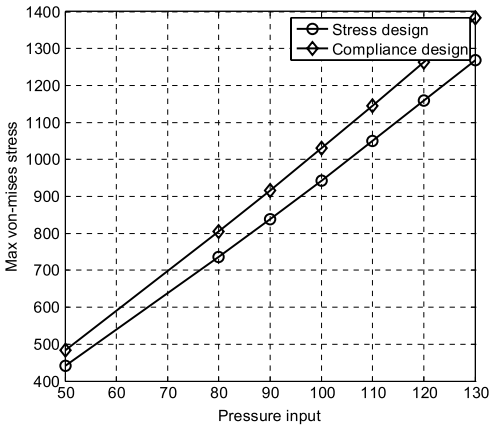

(d)

Fig. 13. Comparison with the compliance minimization problem.

that, unlike what is found in other structural TO, the sensitivity filter of the p-norm actually helps the optimizer to constrain it under a prescribed stress limit because it filters some of the changes of the sensitivity values that are caused by changes in the magnitudes of the stress values. Furthermore, to check whether the results of the present optimization algorithm are optimized from a stress point of view, the compliance minimization problem is solved with the mass usage of Fig. 8(c), i.e., 22.11%, in Fig. 13(b). Fig. 13(c) and (d) compare the compliances and the maximum stresses of the design of Figs. 8(c) and 13(b). From these comparisons, it is recognized that the present method provides optimal layouts that are superior to those of the compliance minimization problems from a stress point of view.

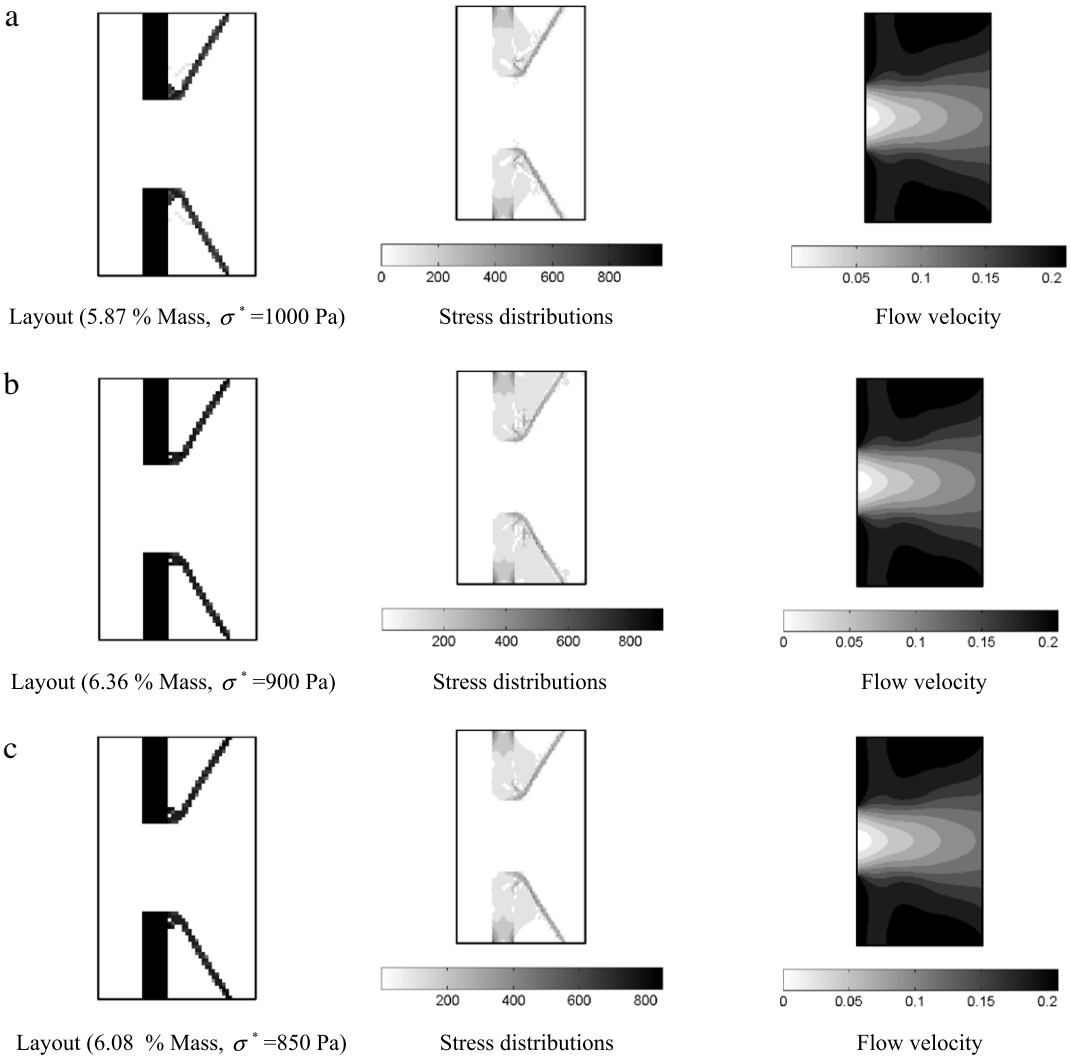

Fig. 14. Optimized layouts with the open channel.

4.2. Example 2: open channel problem

For the second numerical test, we considered a more difficult optimization problem, by setting the middle section of the elastic separator to be a fluid, as shown in Fig. 5(b). Because the thick bar-type elastic structure does not stop the fluidic motion toward the right, the optimization algorithm should determine the optimal interaction boundaries between the fluid domain and the solid domain as they appear in the design domain Ω_{stress}. In the first numerical test, a solid structure with the right design domain was capable of supporting the vertical elastic structure without significantly alternating the fluidic force acting on the surface of the bar-type structure. Consequently, the von-Mises stress inside the objective domain can be easily constrained, which is one of the characteristics of the first numerical example. Conversely, in the second numerical test in Fig. 14, the fluidic force exerted on the interaction boundaries of the design structure took the form of the external force. This fluidic force increases or decreases the magnitudes of the von-Mises stress randomly depending on the intermediate design, which makes the global p-norm stress constraint non-monotonically increase or decrease. Therefore, the optimal mutually coupling boundaries, as well as the elastic structure should be designed using the present optimization algorithm with which the various optimal layouts in Fig. 14 can be obtained. In these designs, the elastic structural members only appear behind the upper and the lower elastic bars so as not to interrupt the fluidic motion toward the right open channel. Unlike the designs in Fig. 8, the

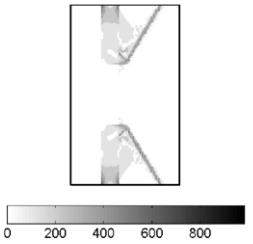

Von-Mises stress (Max: 984 Pa)

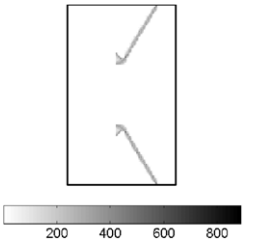

Von-Mises stress $\times\gamma$ (Max: 888 Pa)

(a) Design for Fig. 14(a).

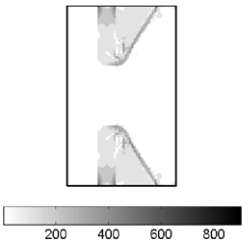

Von-Mises stress (Max: 903 Pa)

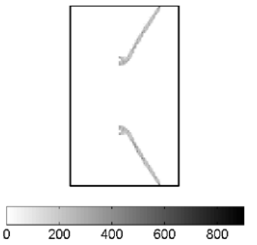

Von-Mises stress $\times\gamma$ (Max: 901 Pa)

(b) Design for Fig. 14(b).

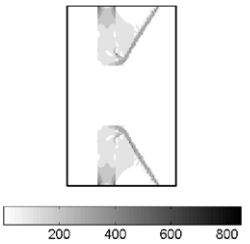

Von-Mises stress (Max: 850 Pa)

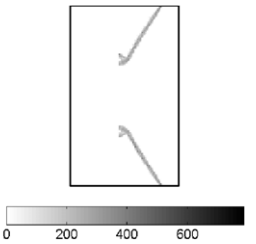

Von-Mises stress $\times\gamma$ (Max: 787 Pa)

(c) Design for Fig. 14(c).

Fig. 15. Vanishing stress constraints for the designs in Fig. 14.

linear combination between mass usages and stress limit is not observed because of the local optima problem. Because the fluidic force is reduced to two thirds of the fluid force, we found that the designs in Fig. 14 utilize less material compared with the designs in Fig. 8 that use the elastic separator. In Fig. 15, the vanishing stress constraints are represented.

Because of the stress singularity issue, the combination of the penalty factors for the Young modulus for the forward analysis and for the stress analysis is important. For the numerical examples shown above, 3 and 0.5 were used for the penalty factors. The other penalty factors are set to an integer ranging from 3 to 5. To show the effects of these penalty values on the optimal designs, Fig. 16 shows some layouts with the different combinations of the penalty factors. Similar designs can be obtained with some different mass usages depending on the values of the penalty factors.

4.3. Example 3: beam on channel

For the third optimization example, we considered the STOM problem on the supporting structure inside the channel of Fig. 17. The elastic bar having dimension of 0.00006 m $\times$ 0.0001 m was located in the middle of the channel. Without this elastic bar, no-structure becomes an optimal solution; however, this is not ideal and it shares similarities with the no-structure issue in that the void structure becomes a local optimum of the STOM in a pure structure problem with fixed forces. By minimizing the compliance subject to the mass constraint, we obtained the design in Fig. 18. By minimizing the volume subject to local stress constraints, the slender bar type obliquely supporting the structures

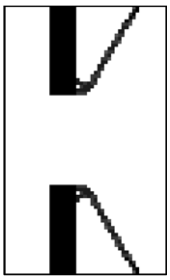

(n: 3, n_s:0.5 , n_{per}: 3, n_{filter} : 5, mass: 6.13%, Max stress: 891, Max p-norm: 870)

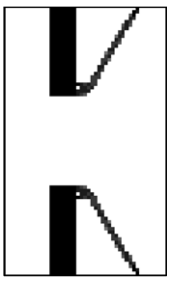

(n: 3, n_s:0.5, n_{per}: 3, n_{filter} : 6, mass: 5.71%, Max stress: 905.94 Pa, Max p-norm: 883.19 Pa)

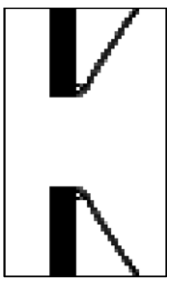

(n: 4, n_s:0.5, , n_{per}: 3, n_{filter} : 4, mass: 5.67%, Max stress: 904.44 Pa, Max p-norm: 895.20 Pa)

Fig. 16. Effects of the penalty factors with an open channel.

can be obtained in Fig. 19. As in the first and the second numerical examples, the design with the smaller stress limit value uses more mass than the other design with the larger stress limit value, which validates the present development for the STOM considering FSI.

4.4. Example 4: internal structure design of an airfoil

For the next optimization example, we design the internal structure of an airfoil due to the aerodynamic force in Fig. 20. For a test, we choose the airfoil called DELFT DU84-132V3 airfoil and make a design domain inside the airfoil. And we artificially make a fluid input as shown in Fig. 20(b) and this fluid input exerts fluidic force to the airfoil. By applying the present approach, the STOM problem with the different stress limits are solved in Figs. 20 and 21. As expected, the internal structures reinforcing the airfoil structure can be obtained (see Fig. 21 and Fig. 22).

4.5. Example 5: drag-based optimization

The purpose of the present study is to present the stress-based topology optimization considering the fluid–structure interaction. Besides this, the present algorithm can be applied to design aerodynamic structure. To show the

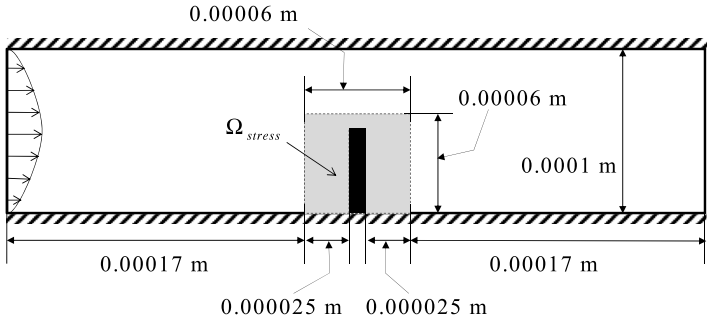

Fig. 17. STOM problem definition inside a channel ($\rho = 1000$ kg/m^3, $\mu = 1.002$ kg/ms, $C_s = 3$ GPa, $v = 0.3$, $C_f = C_s \times 10^{-9}$ N/m^2, $\alpha_{\max} = 10^9$, maximum fluid velocity = 0.3 m/s).

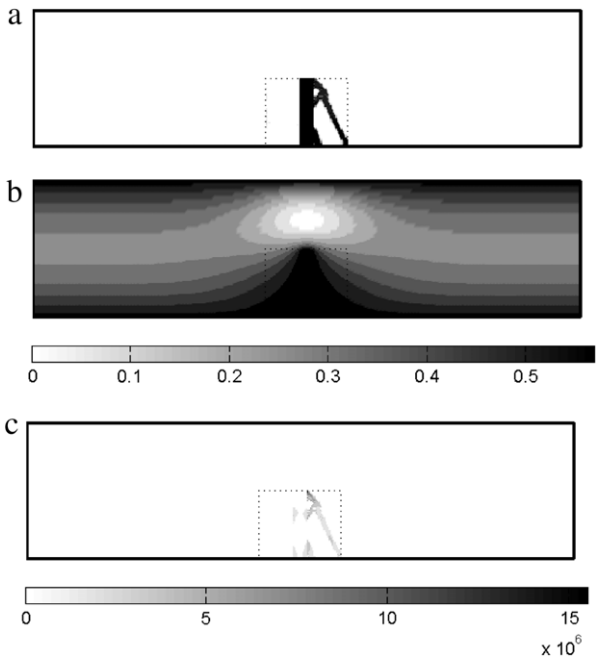

Fig. 18. Compliance minimization problem (Max stress = 1.5514×10^7 Pa, Mass 10%).

applicability of the present approach, we consider the drag-based optimization. First we derive the moment equilibrium equation in x direction for the control volume except the airfoil.

From continuity, the mass ratios of the inlet and the outlet have the following conditions.

$$\dot{m}_1 = \dot{m}_2, \qquad \rho \int_1 u_1 dy = \rho \int_2 u_2 dy \tag{27}$$

where the velocities of the inlet and the outlet are denoted by u_1 and u_2, respectively. The input and the output mass ratios are denoted by $\dot{m}_1$ and $\dot{m}_2$, respectively. The free body diagram in Fig. 23 can be obtained. In the figure, the x-force from the airfoil on the air, the y-force from airfoil on the air, and y-force due to the buoyance are denoted by F_D, F_V, and W_A, respectively. Note that we choose the control volume surrounding the airfoil in a wind tunnel test. From the x-momentum equilibrium equation, the drag of the airfoil can be obtained.

$$-F_D = \rho \left(\int_2 u_2^2(y) dy - \int_1 u_1^2(y) dy \right) b + \left(\int_2 p dy - \int_1 p dy \right) b \tag{28}$$

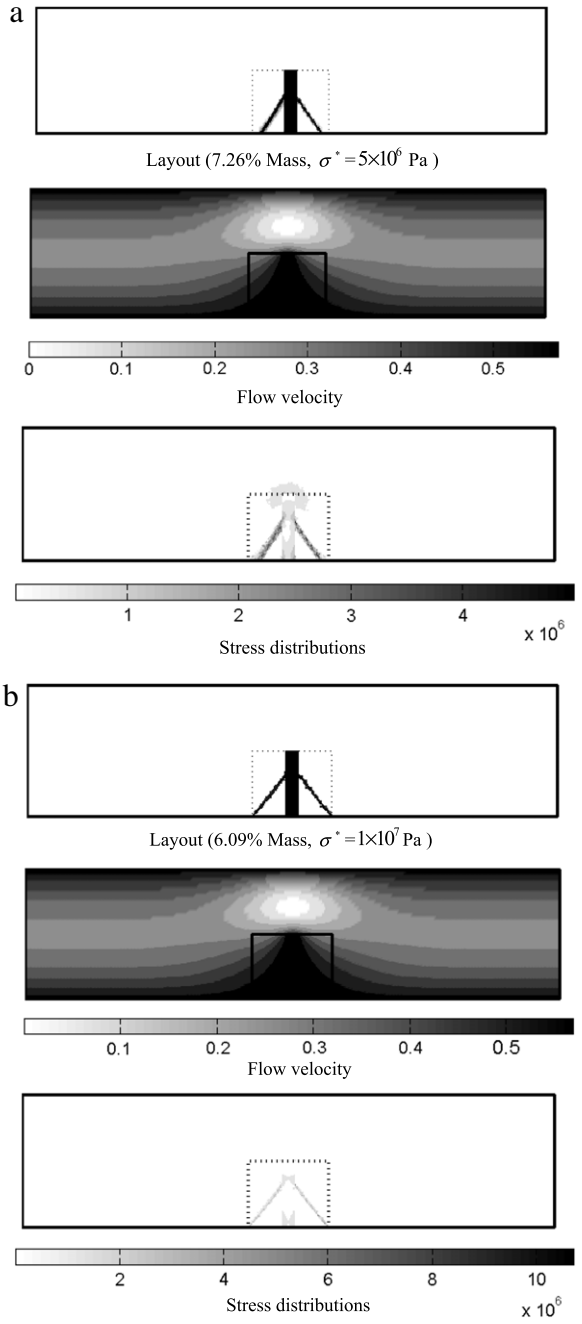

Fig. 19. Optimal layouts for channel fluid.

where the thickness of the airfoil and the wind tunnel, b, is set to 1. In this research, the following optimization problem is considered.

$$\begin{aligned} &\underset{\boldsymbol{\gamma}}{\text{Minimize}}\ F_D \\ &\text{subject to}\ V \leq V^0 \end{aligned} \tag{29}$$

where the allowed mass ratio is set to V^0. Although the problem is not related to the stress-based optimization, it can show one of the possible applications of the present approach. In order to test the effects of the outer design domain

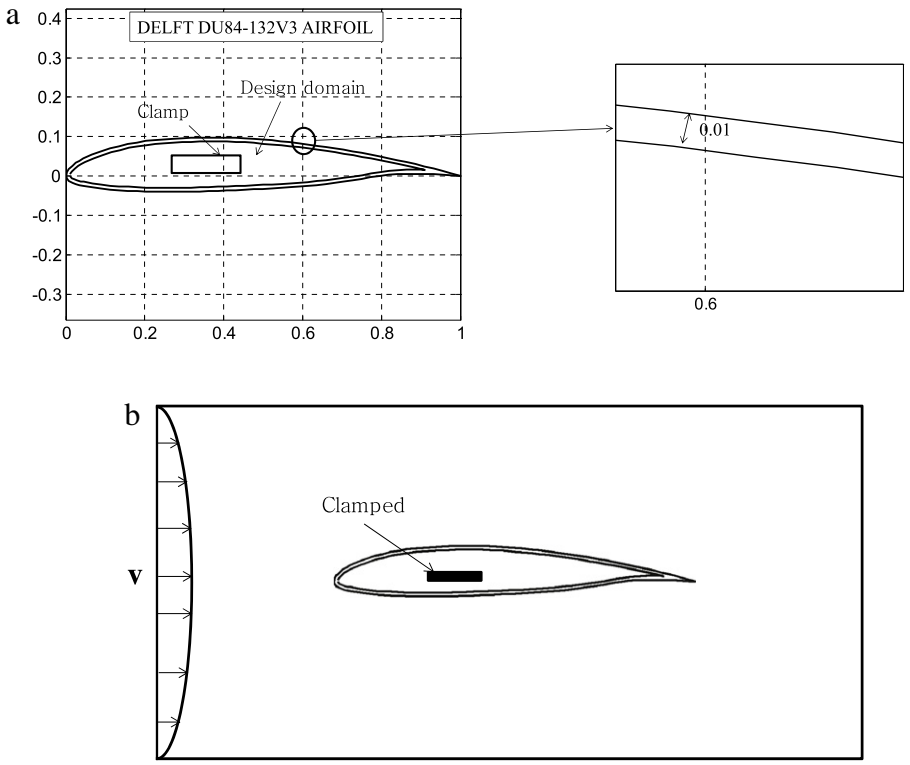

Fig. 20. Stress minimization problem due to the aerodynamic force. (a) The DU84-132V3 Airfoil ($\mathbf{V} = 0.5$ m/s, $\rho = 1$ kg/m^3, $\mu = 1$ Pa s, $C_s = 10^9$ N/m^2, $\nu = 0.3$, $C_f = C_s \times 10^{-6}$ N/m^2, $\alpha_{\max} = 10^9$), and (b) the boundary condition.

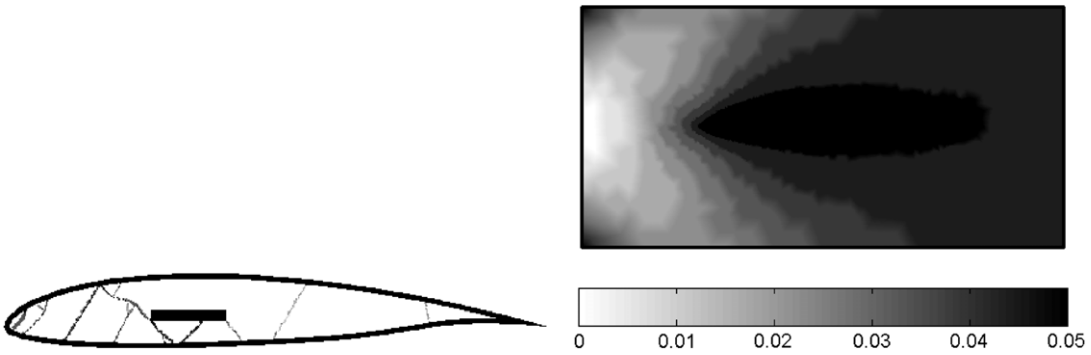

(a) Mass ratio = 2.7800%. (b) Velocity.

Fig. 21. Optimization results with different stress limits. (a) Optimal layout ($\sigma^* = 10$ N/m^2) and (b) velocities.

as well as the inner design domain, the design domains are set as in Fig. 24. To minimize the drag force which is approximately proportional to the cross sectional area, the design variables of the outer design domain become zeros and the internal structures appear to minimize the deflection in Figs. 25 and 26. From an objective point of view, their values are not different to each other. That is because the drag force is approximately proportional to the drag coefficient, the cross section, the fluid density and the square of the fluid velocities.

$$F_D \propto C_{\text{Drag coefficient}} A_{\text{Cross section}} \rho_{fluid} V^2. \tag{30}$$

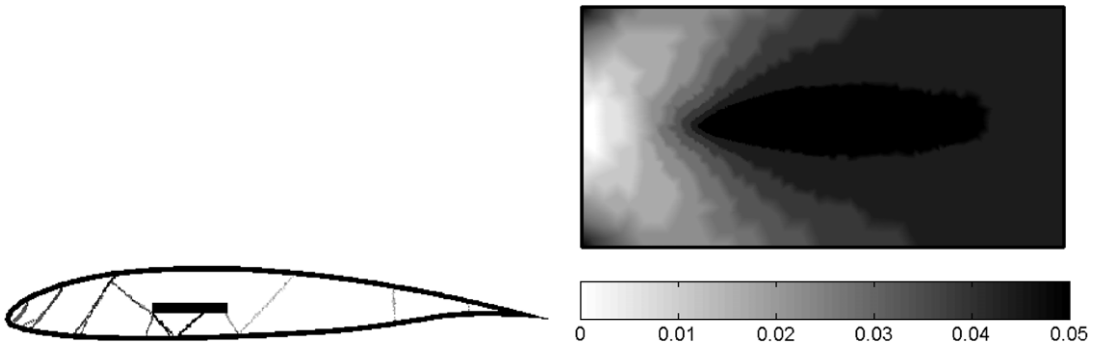

(a) Mass ratio = 3.6206%. (b) Velocity.

Fig. 22. Optimization results with different pressure inputs. (a) Optimal layout ($\sigma^* = 13$ N/m^2) and (b) velocities.

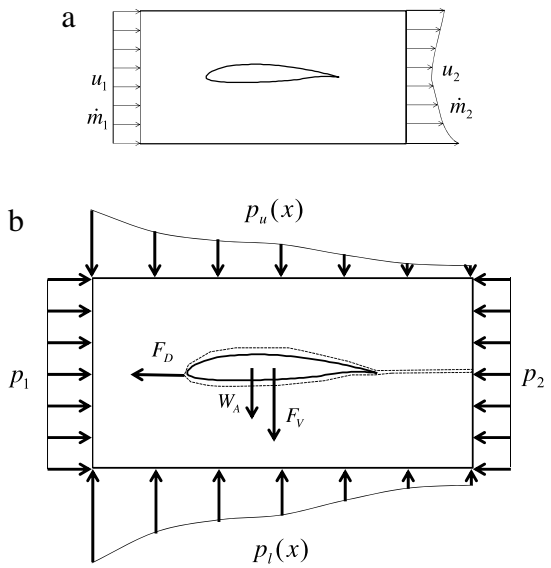

Fig. 23. Drag-based optimization. (a) A propeller (DELFT DU84-132V3 AIRFOIL) inside a channel test section, and (b) free-body diagram of the propeller with the control volume around the airfoil excluding the airfoil.

5. Conclusion

In this study, a new stress-based TO that minimizes the structural volume subject to local stress constraints for an FSI structure was developed. To analyze an FSI system, staggered or monolithic analysis methods have been successfully applied in previous studies; however, these analysis procedures, which require explicit definitions of structure and fluid, become prohibitively complicated in connection with the density-based TO. Because the fluidic forces exerted on a structure change depending on intermediate designs and the governing equations should be interpolated with respect to the design variables, the STOM that considers FSIs remains a critical issue in TO. To solve this intricate TO problem successfully, the monolithic analysis approach, used in conjunction with the Navier–Stokes equation and the linear elasticity equation coupled with the deformation tensor, was employed. To address the singularity issue of STOM, the *qp*-relaxation method setting the different penalizations of the SIMP for the forward analysis and the sensitivity analysis is employed. With the monolithic analysis and the *qp*-relaxation method, the STOM problem minimizing the volume subject to local stress constraints can be solved. Because the interaction boundaries between solid and fluid are subject to change, unlike the STOM with pure structural analysis, the optimization algorithm should determine the interaction boundaries as well as the optimal material distribution, and many local optima exist. It is also observed that the regional constraint method which sorts elements with respect

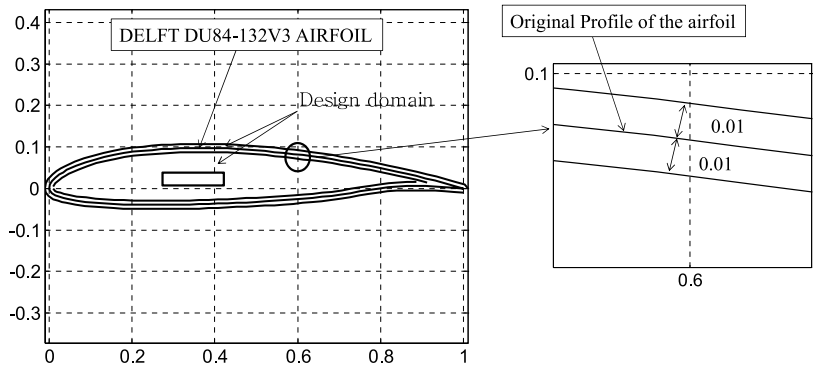

Fig. 24. Design domain of drag-based optimization. ($\rho = 1$ kg/m^3, $\mu_=$1 Pa s, $C_s = 10^9$ N/m^2, $\nu = 0.3$, $C_f = C_s \times 10^{-6}$ N/m^2, $\alpha_{\max} = 10^9$).

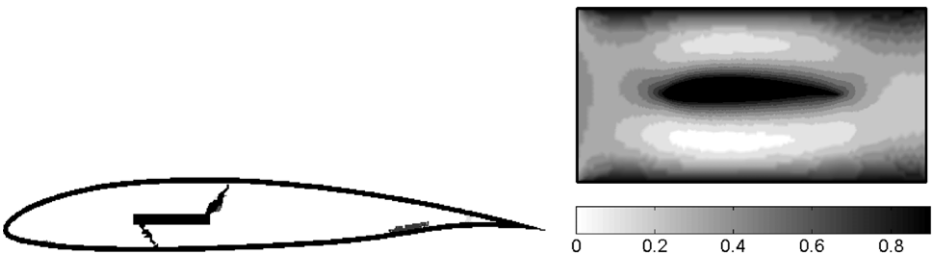

(a) Layout. (b) Velocities.

Fig. 25. Optimization results with different stress limits. (a) Optimal layout (mass ratio = 10%, Drag force = 45.7509 N) and (b) velocities.

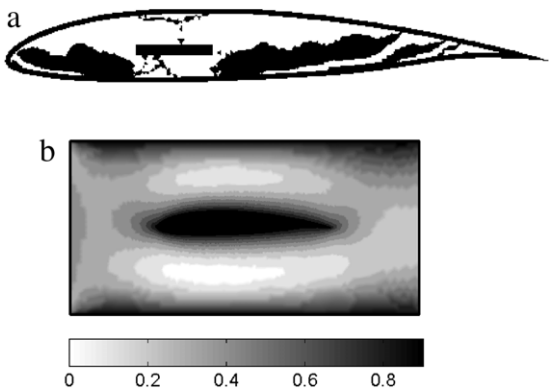

Fig. 26. Optimization results with different stress limits. (a) Optimal layout (mass ratio = 50%, Drag force = 45.7503 N) and (b) velocities.

to the magnitudes of the von-Mises stresses and divides them into groups for calculating the p-norm stress for local stress constraints is not effective in the present optimization formulation because the active–inactive alternations of the regional constraints make FSI analysis and optimization unstable. Alternatively, it may be possible to use the Kreisselmeier–Steinhauser function, which it should be tested in future research. Because of this instability, the one global p-norm stress was implemented. The regional constraint method for an FSI structure should be developed with a view toward future developments because in the present development, locally smoothed designs minimizing the stress concentrations cannot be obtained, which is one of the limitations. Furthermore, it is a very challenging topic to incorporate with the turbulence flow modeled with the Spalart–Allmaras model or the k–ε model. Some other aerodynamic designs should be studied further to show the effect of the stress constraint. In conclusion, this study developed a new STOM problem considering FSI with the monolithic analysis method.

Acknowledgement

This work was supported by the National Research Foundation of Korea (NRF) grant funded by the Ministry of Education, Science and Technology (NRF-2012R1A1A2A10038803).

References

[1] F.J. Blom, A monolithical fluid–structure interaction algorithm applied to the piston problem, Comput. Methods Appl. Math. 167 (1998) 369–391.
[2] S. Kreissl, G. Pingen, A. Evgrafov, K. Maute, Topology optimization of flexible micro-fluidic devices, Struct. Multidiscip. Optim. 42 (2010) 495–516.
[3] D. Makhija, G. Pingen, R.G. Yang, K. Maute, Topology optimization of multi-component flows using a multi-relaxation time lattice Boltzmann method, Comput. Fluids 67 (2012) 104–114.
[4] M. Allen, K. Maute, Reliability-based shape optimization of structures undergoing fluid–structure interaction phenomena, Comput. Methods Appl. Math. 194 (2005) 3472–3495.
[5] G.H. Yoon, Topology optimization for stationary fluid–structure interaction problems using a new monolithic formulation, Int. J. Numer. Methods Eng. 82 (2010) 591–616.
[6] G.H. Yoon, Topological layout design of electro-fluid-thermal-compliant actuator, Comput. Methods Appl. Math. 209 (2012) 28–44.
[7] C. Andreasen, O. Sigmund, Saturated poroelastic actuators generated by topology optimization, Struct. Multidiscip. Optim. 43 (2011) 693–706.
[8] E. Oktay, H.U. Akay, O. Merttopcuoglu, Parallelized structural topology optimization and CFD coupling for design of aircraft wing structures, Comput. Fluids 49 (2011) 141–145.
[9] K. Maute, M. Allen, Conceptual design of aeroelastic structures by topology optimization, Struct. Multidiscip. Optim. 27 (2004) 27–42.
[10] D.M. De Leon, C.E. de Souza, J.S.O. Fonseca, R.G.A. da Silva, Aeroelastic tailoring using fiber orientation and topology optimization, Struct. Multidiscip. Optim. 46 (2012) 663–677.
[11] B. Stanford, P. Ifju, Aeroelastic topology optimization of membrane structures for micro air vehicles, Struct. Multidiscip. Optim. 38 (2009) 301–316.
[12] B.C. Chen, N. Kikuchi, Topology optimization with design-dependent loads, Finite Elem. Anal. Des. 37 (2001) 57–70.
[13] H. Zhang, S.T. Liu, X.O. Zhang, Topology optimization of 3D structures with design-dependent loads, Acta Mech. Sin. 26 (2010) 767–775.
[14] E. Lee, J.R.R.A. Martins, Structural topology optimization with design-dependent pressure loads, Comput. Methods Appl. Math. 233 (2012) 40–48.
[15] H. Zhang, X. Zhang, S.T. Liu, A new boundary search scheme for topology optimization of continuum structures with design-dependent loads, Struct. Multidiscip. Optim. 37 (2008) 121–129.
[16] X.Y. Yang, Y.M. Xie, G.P. Steven, Evolutionary methods for topology optimisation of continuous structures with design dependent loads, Comput. Struct. 83 (2005) 956–963.
[17] O. Sigmund, P.M. Clausen, Topology optimization using a mixed formulation: an alternative way to solve pressure load problems, Comput. Methods Appl. Math. 196 (2007) 1874–1889.
[18] M. Bruggi, C. Cinquini, An alternative truly-mixed formulation to solve pressure load problems in topology optimization, Comput. Methods Appl. Math. 198 (2009) 1500–1512.
[19] E. Lee, K.A. James, J.R.A. Martins, Stress-constrained topology optimization with design-dependent loading, Struct. Multidiscip. Optim. 46 (2012) 647–661.
[20] E.A. Kontoleontos, E.M. Papoutsis-Kiachagias, A.S. Zymaris, D.I. Papadimitriou, K.C. Giannakoglou, Adjoint-based constrained topology optimization for viscous flows including heat transfer, Eng. Optim. 45 (2013) 941–961.
[21] E.A.K.E.M. Papoutsis-Kiachagias, A.S. Zymaris, D.I. Papadimitriou, K.C. Giannakoglou, Constrained topology optimization for laminar and turbulent flows, including heat transfer, in: Proc. EUROGEN, Evolutionary and Deterministic Methods for Design, Optimization and Control, Capua, Italy, 2011.
[22] C.S. Andreasen, A.R. Gersborg, O. Sigmund, Topology optimization of microfluidic mixers, Int. J. Numer. Methods Fl. 61 (2009) 498–513.
[23] M.M. Gregersen, F. Okkels, M.Z. Bazant, H. Bruus, Topology and shape optimization of induced-charge electro-osmotic micropumps, New J. Phys. 11 (2009).
[24] Y.B. Deng, Z.Y. Liu, Y.H. Wu, Topology optimization of steady and unsteady incompressible Navier–Stokes flows driven by body forces, Struct. Multidiscip. Optim. 47 (2013) 555–570.
[25] W. Akl, A. El-Sabbagh, K. Al-Mitani, A. Baz, Topology optimization of a plate coupled with acoustic cavity, Int. J. Solids Struct. 46 (2009) 2060–2074.
[26] C.S. Andreasen, O. Sigmund, Topology optimization of fluid–structure-interaction problems in poroelasticity, Comput. Methods Appl. Math. 258 (2013) 55–62.
[27] M. Bruggi, P. Venini, Topology optimization of incompressible media using mixed finite elements, Comput. Methods Appl. Math. 196 (2007) 3151–3164.
[28] D. Makhija, G. Pingen, R. Yang, K. Maute, Topology optimization of multi-component flows using a multi-relaxation time lattice Boltzmann method, Comput. Fluids 67 (2012) 104–114.
[29] X. Zhang, Z. Kang, Topology optimization of damping layers for minimizing sound radiation of shell structures, J. Sound Vib. 332 (2013) 2500–2519.
[30] S. Zhou, Q. Li, A variational level set method for the topology optimization of steady-state Navier–Stokes flow, J. Comput. Phys. 227 (2008) 10178–10195.

[31] X. Guo, W. Zhang, W. Zhong, Stress-related topology optimization of continuum structures involving multi-phase materials, Comput. Methods Appl. Math. 268 (2014) 632–655.
[32] X. Guo, W.S. Zhang, M.Y. Wang, P. Wei, Stress-related topology optimization via level set approach, Comput. Methods Appl. Math. 200 (2011) 3439–3452.
[33] K.A. James, E. Lee, J.R.R.A. Martins, Stress-based topology optimization using an isoparametric level set method, Finite Elem. Anal. Des. 58 (2012) 20–30.
[34] S.H. Jeong, S.H. Park, D.-H. Choi, G.H. Yoon, Toward a stress-based topology optimization procedure with indirect calculation of internal finite element information, Comput. Math. Appl. 66 (2013) 1065–1081.
[35] J. París, F. Navarrina, I. Colominas, M. Casteleiro, Stress constraints sensitivity analysis in structural topology optimization, Comput. Methods Appl. Math. 199 (2010) 2110–2122.
[36] J. París, F. Navarrina, I. Colominas, M. Casteleiro, Block aggregation of stress constraints in topology optimization of structures, Adv. Eng. Softw. 41 (2010) 433–441.
[37] J. París, F. Navarrina, I. Colominas, M. Casteleiro, Improvements in the treatment of stress constraints in structural topology optimization problems, J. Comput. Appl. Math. 234 (2010) 2231–2238.
[38] S. Amstutz, A.A. Novotny, E.A. de Souza Neto, Topological derivative-based topology optimization of structures subject to Drucker–Prager stress constraints, Comput. Methods Appl. Math. 233–236 (2012) 123–136.
[39] B. Desmorat, Structural rigidity optimization with an initial design dependent stress field. Application to thermo-elastic stress loads, Eur. J. Mech.- A/Solids 37 (2013) 150–159.
[40] C.-Y. Lin, F.-M. Sheu, Adaptive volume constraint algorithm for stress limit-based topology optimization, Comput.-Aided Des. 41 (2009) 685–694.
[41] Y. Luo, Z. Kang, Topology optimization of continuum structures with Drucker–Prager yield stress constraints, Comput. Struct. 90–91 (2012) 65–75.
[42] Y. Luo, M.Y. Wang, Z. Kang, An enhanced aggregation method for topology optimization with local stress constraints, Comput. Methods Appl. Math. 254 (2013) 31–41.
[43] S.J. Moon, G.H. Yoon, A newly developed qp-relaxation method for element connectivity parameterization to achieve stress-based topology optimization for geometrically nonlinear structures, Comput. Methods Appl. Math. 265 (2013) 226–241.
[44] M. Bruggi, On an alternative approach to stress constraints relaxation in topology optimization, Struct. Multidiscip. Optim. 36 (2008) 125–141.
[45] M. Burger, R. Stainko, Phase-field relaxation of topology optimization with local stress constraints, Siam J. Control Optim. 45 (2006) 1447–1466.
[46] M. Bruggi, P. Duysinx, Topology optimization for minimum weight with compliance and stress constraints, Struct. Multidiscip. Optim. 46 (2012) 369–384.
[47] M. Bruggi, P. Venini, A mixed FEM approach to stress-constrained topology optimization, Int. J. Numer. Methods Eng. 73 (2008) 1693–1714.
[48] G.D. Cheng, X. Guo, epsilon-relaxed approach in structural topology optimization, Struct. Optim. 13 (1997) 258–266.
[49] M. Stolpe, K. Svanberg, On the trajectories of the epsilon-relaxation approach for stress-constrained truss topology optimization, Struct. Multidiscip. Optim. 21 (2001) 140–151.
[50] A. Kawamoto, T. Matsumori, T. Nomura, T. Kondoh, S. Yamasaki, S. Nishiwaki, Topology optimization by a time-dependent diffusion equation, Int. J. Numer. Methods Eng. 93 (2013) 795–817.
[51] R.J. Yang, C.J. Chen, Stress-based topology optimization, Struct. Optim. 12 (1996) 98–105.
[52] C. Le, J. Norato, T. Bruns, C. Ha, D. Tortorelli, Stress-based topology optimization for continua, Struct. Multidiscip. Optim. 41 (2010) 605–620.
[53] Q. Xia, T.L. Shi, S.Y. Liu, M.Y. Wang, A level set solution to the stress-based structural shape and topology optimization, Comput. Struct. 90–91 (2012) 55–64.
[54] X. Guo, G. Cheng, K. Yamazaki, A new approach for the solution of singular optima in truss topology optimization with stress and local buckling constraints, Struct. Multidiscip. Optim. 22 (2001) 364–372.
[55] G.Y. Qiu, X.S. Li, A note on the derivation of global stress constraints, Struct. Multidiscip. Optim. 40 (2010) 625–628.
[56] J. Paris, F. Navarrina, I. Colominas, M. Casteleiro, Topology optimization of continuum structures with local and global stress constraints, Struct. Multidiscip. Optim. 39 (2009) 419–437.
[57] P. Duysinx, M.P. Bendsoe, Topology optimization of continuum structures with local stress constraints, Int. J. Numer. Methods Eng. 43 (1998) 1453–1478.
[58] T. Borrvall, J. Petersson, Topology optimization of fluids in Stokes flow, Int. J. Numer. Methods Fl 41 (2003) 77–107.
[59] K. Cai, Q.H. Qin, Z. Luo, A.J. Zhang, Robust topology optimisation of bi-modulus structures, Comput.-Aided Des. 45 (2013) 1159–1169.
[60] K.A. James, H. Waisman, Failure mitigation in optimal topology design using a coupled nonlinear continuum damage model, Comput. Methods Appl. Math. 268 (2014) 614–631.
[61] S.H. Jeong, S.H. Park, D.-H. Choi, G.H. Yoon, Topology optimization considering static failure theories for ductile and brittle materials, Comput. Struct. 110–111 (2012) 116–132.
[62] S.J. Moon, G.H. Yoon, A newly developed qp-relaxation method for element connectivity parameterization to achieve stress-based topology optimization for geometrically nonlinear structures, Comput. Methods Appl. Math. 265 (2013) 226–241.
[63] J. París, I. Colominas, F. Navarrina, M. Casteleiro, Parallel computing in topology optimization of structures with stress constraints, Comput. Struct. 125 (2013) 62–73.
[64] Q. Xia, T. Shi, S. Liu, M.Y. Wang, A level set solution to the stress-based structural shape and topology optimization, Comput. Struct. 90–91 (2012) 55–64.
[65] M.Y.W.Y. Luo, An enhanced aggregation method for stress-constrained topology optimization problems, in: Proc. 10th World Congress on Structural and Multidisciplinary Optimization, Orlando, Florida, USA, 2013.
[66] K. Svanberg, The method of moving asymptotes - a new method for structural optimization, Int. J. Numer. Methods Eng. 24 (1987) 359–373.